Highly deformable hydrostatic bearings using a single closed fluid cell

Sonneveld, Dave D.; van Ostayen, Ron A.J.

DOI
10.1177/13506501251315977

Publication date
2025

Document Version
Final published version

Published in
Proceedings of the Institution of Mechanical Engineers, Part J: Journal of Engineering Tribology

Original Article

Institution of MECHANICAL ENGINEERS
Journal of ENGINEERING TRIBOLOGY

Proc IMechE Part J:
J Engineering Tribology
1–13

DOI: 10.1177/13506501251315977
journals.sagepub.com/home/pij
Sage

Highly deformable hydrostatic bearings using a single closed fluid cell

Dave D. Sonneveld[1] and **Ron A.J. van Ostayen**[1]

Abstract

The applications where fluid film bearings are used to guide high loads over wavy surfaces are limited. This because current designs of fluid film bearings often consist either of rigid embodiments that are unable to adapt to varying surface curvatures to form the required thin fluid film, or of compliant designs that have been designed to allow only for small deformations. This work discusses the requirements to design highly deformable fluid film bearings and introduces two metrics to compare their performance. Additionally, it introduces a compliant cell that is filled with an incompressible fluid as a design element to obtain both a high load capacity and sufficient deformability for such bearings. This closed fluid cell is also implemented in a 2D axi-symmetric hydrostatic bearing concept, that is numerically modelled and validated by experiments with a prototype. The simulations and prototype show that it is able to operate on surfaces with a hundred times higher curvature than has been analysed in previous studies.

Keywords

Highly deformable hydrostatic bearing, elastohydrostatic lubrication, compliant closed cell, deformable bearing metrics

Introduction

The use of bearings is essential to achieve a smooth motion and long lifespan in machinery. Common types are slider, roller and fluid film bearings. Fluid film bearings avoid all mechanical contact by forming a thin fluid film between the two sliding surfaces. This makes them superior in terms of load capacity, wear and fatigue. Classic designs however are rigid and can only form the thin film on surfaces of constant and uniform curvature, as in journal and thrust bearings. Applications that require a bearing to travel along an undulating surface or a path with a non-uniform curvature therefore often use roller bearings. This is typically seen in cam follower systems to translate the rotational motion of a wavy cam into a linear motion of the follower, as seen in for instance radial piston pumps. The economics of scale make it interesting to scale up such systems to achieve higher power ratings, for example to increase the energy yield in wind turbines.[1–3] But scaling the power also increases the load on machine components. A study on a 600 kW radial piston pump already showed that the contacts in the rollers are the limiting factors in the lifetime of the complete system.[4] A valid alternative for the bearing between cam and cam follower in this high load application is therefore desired.

Existing fluid film bearings provide no alternative for the rollers due to their inability to form a thin film on surface geometries with a non-uniform curvature. A solution for this could be to add compliance to the bearing slider so it can adapt its shape. Previous studies already introduced compliance for this purpose, mostly in the form of a rubber support. This has been applied as a pivot to allow hydrostatic or hydrodynamic pads to tilt for higher load capacities[5,6] and directly as a deformable pad.[7–9] The deformable pads have been analysed for waviness amplitudes between 1-100 times the average film height, with a maximum amplitude of 10mm.[9] Only one study that proposed a design with multiple pads analysed slightly larger amplitudes.[10] A functional stroke for large scale cam follower systems however, is expected to be ≥ 1000 times the film height, which is an order of magnitude higher than realized in the current studies. The question therefore arises whether highly deformable, single pad fluid film bearings can be designed to operate on wavy surfaces of such amplitude.

An important first step to answer this question is to identify how a higher deformability can be integrated with the operating conditions of fluid film bearings.

[1]Department of Precision and Microsystems Engineering, Delft University of Technology, The Netherlands

Corresponding author:
Dave D. Sonneveld, Department of Precision and Microsystems Engineering, Delft University of Technology, 2628CD Delft, The Netherlands.
Email: d.d.sonneveld@tudelft.nl

This is discussed in the beginning of this paper, resulting in three general design requirements. The required deformation to adapt the bearings to a wavy surface can be divided into two parts: a rotation of the pad to match the average surface incline (i.e. the first order unevenness) and a change in its shape to match the surface curvature (i.e. the second order unevenness). The limitation of the existing technology is to obtain this change in shape, which is what the remainder of this paper focuses on by example of a two-dimensional (2D), axi-symmetric design case. So in continuation on the general requirements, two metrics are introduced to quantify the adaptability of bearings in this case and to allow a comparison between designs in general. The potential of a compliant cell that is filled with an incompressible fluid[11] for deformable fluid film bearings is discussed and as a first step it is implemented in the design of a hydrostatic bearing. The intended working principle of this design is described and a numerical model is presented with an analysis of the design's behaviour on wavy surfaces. Finally, the model is validated with experiments.

Method

The method first describes the general design requirements and metrics for highly deformable bearings. This is followed by the conceptual design, its implementation and analysis in a numerical model and finally the experimental validation.

General design requirements

The generation of a high load capacity in fluid film bearings depends on the pressure build-up in the thin fluid film. This is commonly studied in elastohydrodynamic lubrication (EHL), where the height and pressure are strongly coupled due to the elastic deformation or compliance of the sliding surfaces.[12] Previous studies that introduced compliance mainly focused on small deformations that ensure the preservation of the thin film and thus the pressure. Adding high deformability allows these bearings to adapt to larger surface variations, although it can also initiate undesired deformations due to the high loads acting on the bearing.[9] It is therefore important to identify the general requirements to combine a high load capacity with a high deformability.

The first requirement relates to the stiffness of the bearing. Traditional fluid film bearings consist of rigid embodiments with a high stiffness to transmit high loads and prevent any pad deformations that affect the performance. This high overall compressive stiffness is still desired in deformable fluid film bearings to prevent a collapse under high loads and to maintain a track following ability in cam follower systems. Additionally though, it is desired that the bearing can passively adapt its shape to avoid the complexity of an actuation mechanism. The only stimuli to achieve this in a passive bearing are the changes in film pressure that result from variations in the film height when the bearing moves over a wavy surface. These changes however can be relatively small, especially in a recess or near the edges of the bearing where the film always approaches the ambient pressure. A low internal stiffness is therefore desired at the surface of the pad to make sure that even small changes in the film pressure will result in a modified bearing shape. With respect to the bearing stiffness, it is thus required to design for both a high external and low internal stiffness.

Secondly, the bearing should be able to form an equilibrium with the film pressure. In hydrostatic bearings for example, the film pressure always decreases monotonically from the supply to the outflow at the edges of the bearing. In rigid bearings this is not important as the higher pressure in the central part can lift the entire bearing. A deformable bearing however, could fold itself around the high pressure zone and squeeze the flow at the edges of the bearing. To prevent this, the bearing should exert a comparable pressure on the fluid as the film pressure does on the bearing. It is therefore important that the applied load on the bearing is distributed to the surface of the pad in a profile that can be matched by the fluid film. Ideally, this can even be used to design for a specific film height profile by matching the load distribution to the film pressure that is expected from that profile, as shown in literature for small deformations.[9]

Lastly, it is important to consider the type of structure that can be used. It is undesired to use any form of mechanism consisting of multiple discrete elements that are connected by classic joints, as this re-introduces wear and fatigue between the individual mechanical components in the support. The bearing should therefore consist of a compliant system that only changes its geometry by elastic deformation, as commonly seen in compliant joints.[13]

Metrics

The functionality of fluid film bearings to operate on varying surface curvatures also requires a quantification method to analyse and compare their performance in doing so. Hence, this section discusses some of the currently used metrics and proposes two adapted metrics, of which the first is focused on hydrostatic bearings for the example in this study.

Common metrics that remain useful to analyse deformable (hydrostatic) bearings are the load capacity, minimum film height, flow and operating power.[14] These metrics however only provide indirect information about the film and do not describe how well a bearing adapts to the surface. A better parameter for this is the land width, which is the length of the film with a relatively small film thickness and large pressure drop. In rigid bearings this land width is clearly defined by the geometry as shown in Figure 1(a). The land width size can be tuned to obtain a maximum load capacity with minimum power[15] but is preferably not too small such that sufficient flow

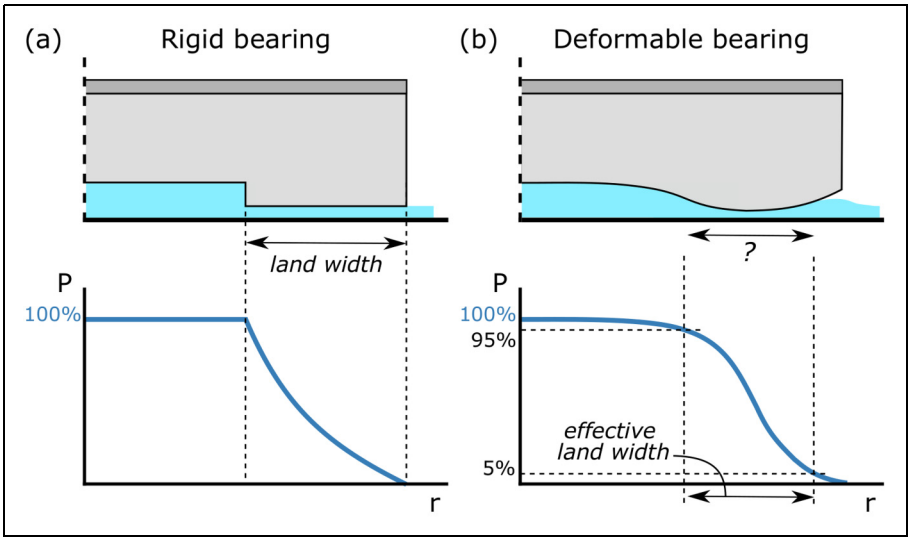

Figure 1. The land width in rigid bearings and the new effective land width metric that is based on the film pressure *P*.

resistance can be generated in the film at an acceptable minimum film height. The latter is also important on surfaces of varying curvatures, which makes the land width a suitable metric for the adaptability. The problem is that deformable pads can result in a film profile without a clear land width, as seen in Figure 1(b). To solve this, we introduce the '*effective land width*' α: a metric that uses the pressure drop in the land area to identify the effective width of the thin film. For the 2D axi-symmetric case it is defined as the radial distance over which the film pressure drops from 95% to 5% of the inlet pressure, with margins of 5% to account for the pressure loss in the recess and diverging outflow of the bearing. A schematic of the metric is shown at the bottom of Figure 1(b).

A remark on the effective land width is that it only defines the adaptability of a bearing to a surface, without specifying anything about that surface. A metric for the unevenness is thus important to indicate how deformable a bearing is or should be to reach a certain adaptation (e.g. a specified effective land width). Ideally, such a metric is dimensionless to be able to compare bearings and application surfaces of different sizes. A previous study already stated that high deformable bearings should be able to deform >10% of the undeformed bearing height and >100 times the average film height.[9] The disadvantage however is that the definitions ignore the bearing length over which the compression is achieved, which relates to the unevenness of the surface. Next to the initial shape, a metric for the unevenness should therefore be formulated relative to the bearing length. For the analysis of bearing designs, it is assumed that the surface unevenness can be described using a uniform radius of curvature. The radius of curvature can then be used as metric for the unevenness, which is introduced in the '*dimensionless surface curvature*' $\overline{k}$ as in

$$\overline{k} = L_b \cdot \left(\frac{1}{R_s} - \frac{1}{R_n} \right) \tag{1}$$

where L_b is the bearing length, R_s the radius of curvature of the surface that is analysed and R_n the neutral radius of curvature for which the bearing is designed. The sign conventions and a schematic of how this metric generalizes a bearing situation to a single value of $\overline{k}$ are shown in Figure 2.

Conceptual design

A promising structure to meet the design requirements is a compliant closed cell that is filled with an incompressible fluid. Its introduction as a universal joint showed that closed fluid volumes have the potential to combine a high load capacity with relative high deformability.[11] A similar design is therefore proposed for a deformable hydrostatic bearing, as shown in Figure 3. It contains a closed fluid volume similar to the universal joint, but it has a separate fluid supply for the film and uses the bottom cell wall as its hydrostatic pad. Based on this cross section, the design motivation and its expected working principle are elaborated in this section.

The core idea of the design is to use an incompressible fluid in a thin walled cell.[11] The incompressibility enforces that the internal volume remains constant. A compression of the cell by an external load therefore demands a lateral expansion of the cell, which is resisted by the tensile stiffness of the cell wall. This creates an internal pressure that counteracts the external load and provides both a load carrying capacity and bearing stiffness. The fluid however can deform without residual stresses. The adaptation of the cell wall to the surface therefore only depends on its bending stiffness, which is relatively low for thin enclosures. A closed cell could thus obtain both the overall (external) compression stiffness and low (internal) deformation stiffness. Additionally, fluids have the property that their internal pressure is constant in all directions and throughout their volume. This allows the fluid to press equally on the entire hydrostatic pad from above, even when the

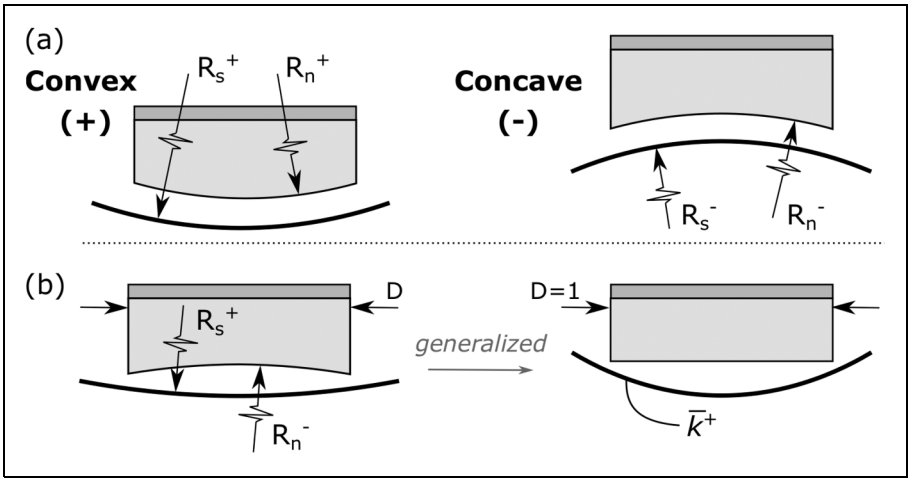

Figure 2. (a) Sign convention for the radii of curvature of the surface R_s and bearing R_n. (b) Example of the dimensionless surface curvature $\bar{k}$ that generalizes the required deformability.

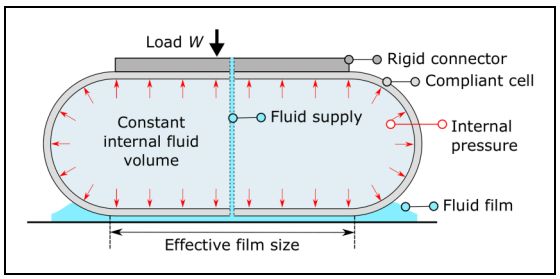

Figure 3. Concept design for a deformable hydrostatic bearing using a closed cell that is filled with an incompressible fluid.

cell wall is deformed. Such a constant pressure matches with the rectangular pressure profile of recessed bearings and gives two advantages. It is beneficial to obtain a high load capacity and it indicates that the load on the bearing is distributed to the cell wall in a pressure profile that can be matched by the fluid film. The latter satisfies the second requirement that an equilibrium can be formed between the fluid film and the bearing. Together with the compliant nature of the cell, this concept thus meets the general requirements.

The working principle of the cell to adapt to different curvatures is based on the difference between the pressures in the internal fluid and the fluid film. The internal pressure can be approximated with the division of the external load by the area of the rigid connector normal to it. For a given load W, this internal pressure is thus constant. The film pressure however changes for different surface curvatures, which is explained by the size of the film. The '*effective film size*' can be defined as the size of the film that delivers a useful pressure contribution to the load capacity. The film pressure drops significantly where the film diverges, which gives an effective film size as seen in Figure 3. On convex surfaces, this effective size increases as the narrow parts of the film move outward along the curvature of the cell, which is shown in Figure 4. To deliver the same load capacity, the average film pressure thus decreases. This change in the film pressure results in a pressure difference over the cell wall that deforms the cell wall into the convex surface. Similarly for concave surfaces, the effective film size decreases which results in a higher film pressure that deforms the cell wall upwards.

Numerical model and analyses

The conceptual design has been implemented in a numerical model to analyse its behaviour on different curvatures. This section describes the set-up and assumptions of this model, its numerical implementation and the performed analyses.

The modelling approach is largely based on the study that introduced the closed cell as a compliant joint,[11] with the addition of the Reynolds equation to model the fluid film. A representation of the modelled 2D axisymmetric system is shown in Figure 5(a). The undeformed geometry of the closed cell is described by its flat diameter D, nominal height H and wall thickness T. Together, it can be derived that these parameters define the initial revolved volume V_0 by

$$V_0 = \frac{\pi(H-T)}{24}\left(6D^2 + 3\pi D(H-T) + 4(H-T)^2\right) \quad (2)$$

The hydrostatic pad of the closed cell is separated from the surface by a film thickness h, which depends on the surface geometry that curves upwards or downwards according to

$$z_s = R_s - R_s \cdot \sqrt{1 - \left(\frac{r}{R_s}\right)^2} \quad (3)$$

where z_s is the surface height at radial coordinate r and R_s the surface radius as defined in Figure 2.

The model itself consists of four main equations: the linear elasticity equations, an internal volume constraint,

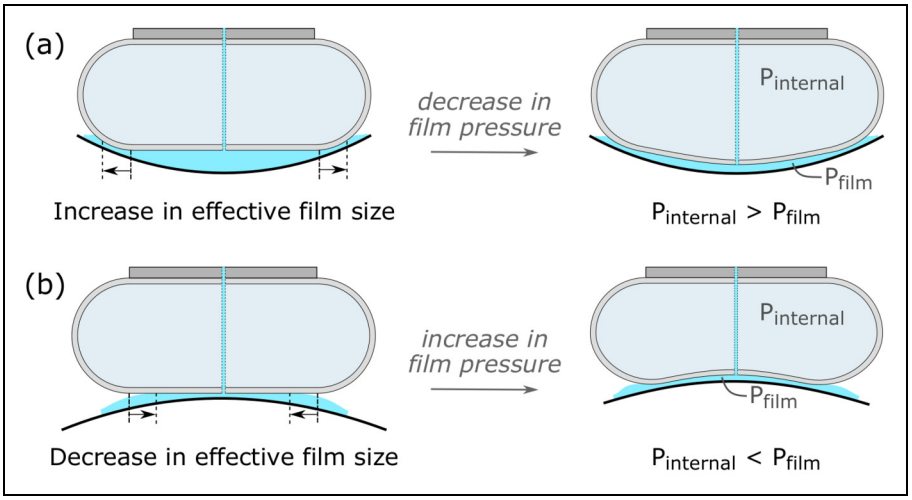

Figure 4. Schematic of how the effective film size changes on (a) convex and (b) concave surfaces, resulting in a different film pressure that causes the hydrostatic pad to adapt.

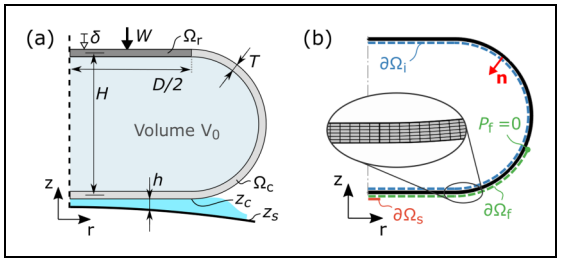

Figure 5. (a) Schematic of the modelled 2D axi-symmetric system and (b) the meshed domains with indicated boundaries.

a load balance and the Reynolds equation. These equations are all solved simultaneously to determine the elastic deformation of the cell, the internal pressure P_i, the displacement δ of the rigid connector and the film pressure P_f. The linear elasticity equations are applied to the cell wall domain Ω_c in Figure 5(a). Although geometric nonlinearities are included, linear elasticity is used to focus on the concept's general behaviour and not the effect of a specific material. The top horizontal cell domain Ω_r is hereby assumed rigid due to its fixation to the rigid connector and only allowed to translate vertically by the axi-symmetry of the model. The internal volume constraint is used to model the internal pressure P_i that is applied on the domain boundary $\partial\Omega_i$ in Figure 5(b). It adjusts the pressure P_i until the internal volume V matches the initial volume V_0, which is defined by

$$\frac{V}{V_0} - 1 = 0 \tag{4}$$

To analyse the volume V in any deformed configuration, the divergence theorem can be used,[16] implemented here as

$$V = -\int_{\partial\Omega_i} (n_r \cdot \pi r^2)\mathrm{dl} \tag{5}$$

where n_r represents the radial component of the normal unit vector $\mathbf{n}$, indicated in Figure 5(b), and l the length of $\partial\Omega_i$.

The equation regarding the load balance governs the equilibrium between the load W and the vertical contribution of the film pressure. This equation however is implemented indirectly by applying load W on the rigid domain Ω_r, which influences the cell displacement δ and thus the film pressure until an equilibrium is obtained in the linear elasticity equations. The Reynolds equation is lastly used on the outer boundary $\partial\Omega_f$ in Figure 5(b) to model the film pressure P_f. For this equation it is assumed that the pressure across the film is constant, that the fluid is incompressible and shows Newtonian behaviour, and that steady-state and isothermal conditions apply. This is considered acceptable for a general analysis of the concept and applicable to the experimental conditions that use water as the lubricating fluid at low loads. With the assumptions, the Reynolds equation in polar coordinates reduces to[15]

$$\frac{\partial}{\partial r}\left(-\frac{\pi r h^3}{6\eta}\frac{\partial P_f}{\partial r}\right) + \frac{\partial}{\partial z}\left(-\frac{\pi r h^3}{6\eta}\frac{\partial P_f}{\partial z}\right) = 0 \tag{6}$$

where η is the dynamic viscosity and h is simplified to

$$h = z_c - z_s \tag{7}$$

with z_c indicating the height of the hydrostatic pad as shown in Figure 5(a). The z-term in equation (6), uncommon in most formulations, is used here because the partial differential equation is defined on the curving edge of the cell and thus contains a non-negligible pressure gradient in the vertical direction. The fluid film supply is defined on the boundary $\partial\Omega_s$, indicated in Figure 5(b). In this research, we propose the use of a modified restrictor relation that regulates flow Q by

$$Q = C_d A_0 \left(\frac{2(P_s - P_f)}{\rho}\right)^f \tag{8}$$

where C_d is the orifice discharge coefficient, A_0 the cross sectional area of the restrictor, P_s the supply pressure and ρ the fluid's density. The power factor f, which is 0.5 for ideal orifice restrictors and used as such in the numerical

analysis, is presented as a variable to better describe restrictors that behave in between the linear and orifice regime, as further elaborated in the experimental validation. Finally, the model has a zero pressure boundary condition at the right end of the boundary domain $\partial\Omega_f$ to match the ambient pressure. The resulting pressure P_f from the Reynolds equation is applied as pressure load on the boundary $\partial\Omega_f$ to couple the partial differential equation to the linear elastic domain Ω_c.

The equations have been implemented in the finite element method (FEM) software package COMSOL Multiphysics.[17] In this model, the mesh is built with rectangular elements parallel to the cell wall as no significant gradients are expected over its thickness. An example of this mesh and its size, which has been confirmed by mesh convergence studies, is shown in Figure 5(b). A third-order (cubic) discretization is used for the line elements on $\partial\Omega_f$ to model the Reynolds equation and a second-order (quadratic) discretization for the elements in Ω_c for the remaining equations. To obtain convergence, the numerical procedure is divided in three steps. First, only the Reynolds equation is solved for the initial geometry, in which the cell's pad z_c is placed several times the expected film height above the surface z_s. This results in a low film pressure P_f that is activated as boundary load in the second step, together with the internal pressure P_i and the internal volume constraint. The rigid domain Ω_r is hereby fixed in space. In the third step, this fixed constraint is removed and the load W is activated with a low value to reach a converged starting solution for the full system of equations. From there, the load and curvature can stepwise be increased and changed.

With the model, the steady state behaviour of the closed cell hydrostatic bearing has been computed on a convex and concave surface for increasing loads and curvatures. To show how this behaviour differs from the conventional bearings, a comparison is made to a rigid and recessed thrust bearing that was simulated in equal conditions. The parameters for this comparison are shown in Table 1. To generalize the analysis, a dimensionless approach has been used. The parameters of the supplies are further tuned such that on a flat surface both bearings fly at the minimum film height h_0 at the baseline load W_0 and a pressure ratio of $\beta = 0.5$. With respect to the flexibility of the cell wall, both the Young's modulus and cell thickness are important. A measure for the flexibility is the flexural rigidity, which by scaling to the load and diameter of the bearing can be formulated dimensionless by

$$\overline{G} = \frac{1}{WD} \cdot \frac{E \cdot T^3}{12(1-\nu^2)} \tag{9}$$

where $\overline{G}$ is the dimensionless flexural rigidity, E the Young's modulus and ν the Poisson ratio. The Young's modulus and cell thickness for the comparison are based on $\overline{G} = 5 \cdot 10^{-5}$, which is similar to the parameters that proved to work in the experimental validation. The effect of the dimensionless flexural rigidity is further reflected upon in the discussion.

Experimental validation

To validate the numerical model, a prototype was built and tested. This section briefly describes the fabrication, the experimental setup and the measurement procedure.

The experimental setup parameters are shown in Table 2. To fabricate the bearing, first the top and bottom halves of the cell are moulded from a silicone rubber. The moulds for this are mainly made with a fused deposition modelling (FDM) printer, except for the one for the hydrostatic surface that is made with a stereolithography (SLA) printer to obtain a smoother surface. The upper half of the cell is then clamped by two 3D-printed plates to form the rigid connector,

Table 1. Parameters for a numerical comparison between an initally flat closed cell and a rigid, recessed thrust bearing.

Parameter	Description	Value	Unit
General			
D	Bearing diameter	1	[−]
A_b	Bearing area	$\pi D^2/4$	[−]
W_0	Baseline load	1	[−]
h_0	Baseline film height	1/1000	[−]
ρ	Fluid density	1	[−]
η	Fluid dynamic viscosity	1	[−]
f	Orifice power factor	0.5	[−]
Recessed thrust bearing			
D_r/D	Rel. recess diameter	0.5	[−]
h_r/h_0	Rel. recess depth	10	[−]
$P_s \cdot (A_b/W_0)$	Rel. supply pressure	3.7	[−]
$C_d A_0/h_0^2$	Rel. restrictor parameters	$8.19e^{-4}$	[−]
Closed cell bearing			
H/D	Rel. cell height	0.5	[−]
T/D	Rel. cell thickness	1/100	[−]
$E \cdot (A_b/W_0)$	Rel. Young's modulus	353.4	[−]
ν	Poisson ratio	0.49	[−]
$P_s \cdot (A_b/W_0)$	Rel. supply pressure	1.74	[−]
$C_d A_0/h_0^2$	Rel. restrictor parameters	$6.75e^{-3}$	[−]

Table 2. Parameters for the experimental validation.

Parameter	Description	Value	Unit
D	Cell diameter	60	mm
H	Cell height	30	mm
T	Cell thickness	1.5	mm
E	Cell Young's modulus	1.0	MPa
ν	Poisson ratio	0.49	–
P_s	Supply pressure	0.8	bar
C_d	Orifice coefficient	0.34	$(m/s)^{1-2f}$
A_0	Orifice area	3.66	mm^2
f	Orifice power factor	0.58	–
W_0	Baseline load	100	N
ρ	Density (water)	1e3	kg/m^3
η	Dynamic viscosity (water)	1	mPa · s
R_s	Surface curvature radius	0.1515	m

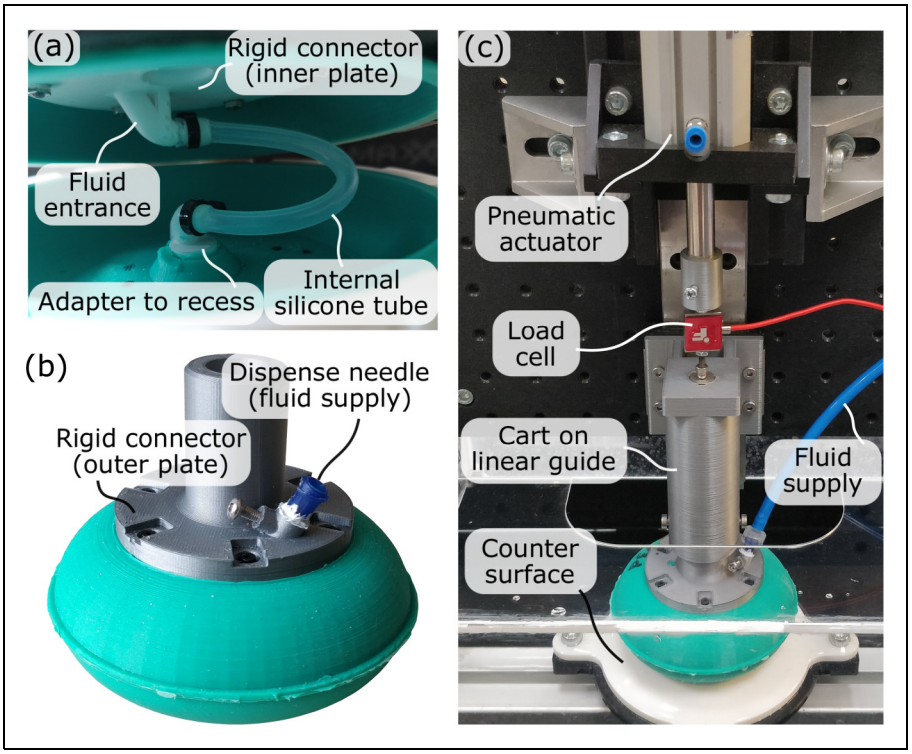

Figure 6. Picutures of (a) the prototype's internal structure, (b) the assembled prototype and (c) the experimental setup.

which is connected via a tube to an integrated adapter in the bottom half for the supply to the fluid film. A picture of this internal structure is shown in Figure 6(a). Next, the two halves are bonded together with the same silicone rubber, after which the internal volume is cleared from air and filled with water via a needle through the top of the cell. Finally, a dispensing needle is installed on the rigid connector to function as the orifice restrictor and coupling to the external fluid supply. A picture of the resulting prototype is shown in Figure 6(b).

In the experimental setup, the prototype is mounted on a vertical linear guide and pressed against a counter surface with a pneumatic actuator as shown in Figure 6(c). A load cell (Futek LSB201-QSH02035) is placed between the actuator and bearing to measure the applied force, to which the weight of the bearing needs to be added due to the fact that the bearing is positioned below the sensor. The counter surface is interchangeable to allow tests on different curvatures. The pressurised fluid for the measurements is provided by an external pump, of which the volumetric flow and pressure are respectively measured by a magnetic-inductive flow metre (ifm SM6000) and pressure sensor (ifm PT5415) before entering the restrictor.

As mentioned below equation (8), a modified relation for the flow through the restrictor is proposed with a variable power f. Standard orifice restrictors have a short hole with sharp edges to obtain an optimal flow resistance, with $f = 0.5$ and C_d-values around 0.6.[15,18] The dispense needle however contains more rounded edges at its entrance, which reduces the inertia effects that cause the square root relation in ideal orifice restrictors, and a longer shaft that is similar to a linear, capillary restrictors. A more linear flow resistance of the needle is therefore expected, although the standard linear relation is not suitable as the Reynolds number largely exceeds that of a laminar flow to base the resistance only on viscous forces. With the variable power f, a behaviour that is in between the ideal orifice and capillary restrictors can be fitted in combination with the C_d-value. The fitted values for the dispense needle in this setup, which were determined with a separate flow measurement, are shown in Table 2.

With the experimental setup, the steady state volumetric flow of the bearing can be measured at a specific load case. For such measurements, the fluid supply is first activated and tuned until the necessary supply pressure is set, before the load is increased. When both the supply pressure and load are at the desired operating conditions, the flow is measured for 10 seconds. This was repeated three times for increasing loads on a flat glass plate and both a convex and concave SLA-printed surface to validate the numerical model.

Results

Numerical analyses

The results of the numerical comparison between the rigid, recessed thrust bearing and the closed cell bearing with the parameters from Table 1 are shown in Figures 7 to 9 and consist of two data representations. The first in Figure 7 displays the load capacity of both bearings

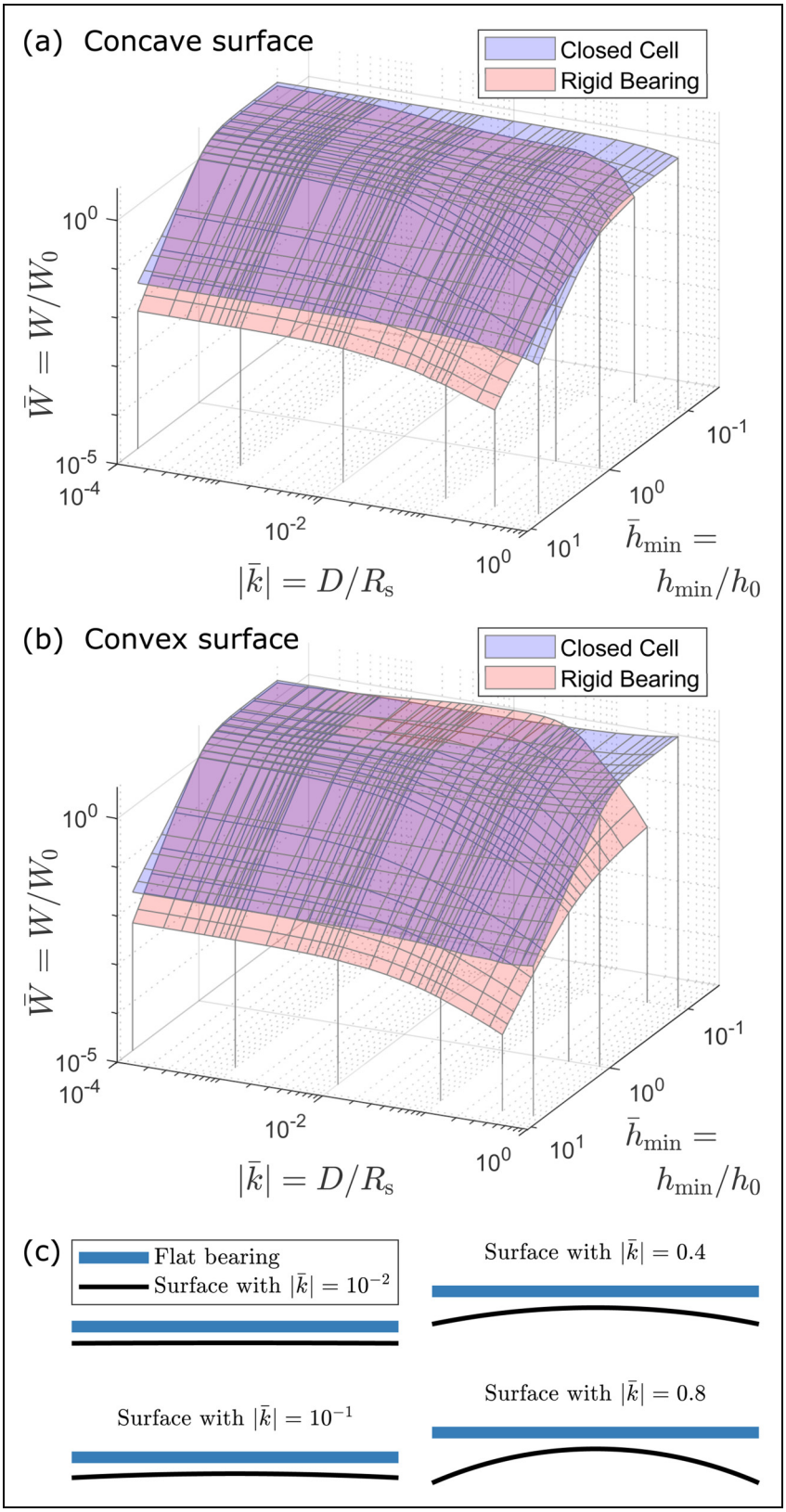

Figure 7. (a,b) Surface plots showing the load capacity W of the closed cell bearing and rigid, recessed thrust bearing for different minimum film heights h_{min} on varying concave and convex curvatures $\bar{k}$. The loads are scaled to the baseline load W_0 and the film heights to the baseline film height h_0. (c) Examples on scale of different magnitudes of the dimensionless curvature $\bar{k}$.

for a range of minimum film heights and curvatures, which provides a general comparison in performance over a wide operating range. Some examples of the curvature magnitude $\bar{k}$ are added in part c of this figure to illustrate its significance. The second analysis in Figure 8 shows how the minimum film height, flow and

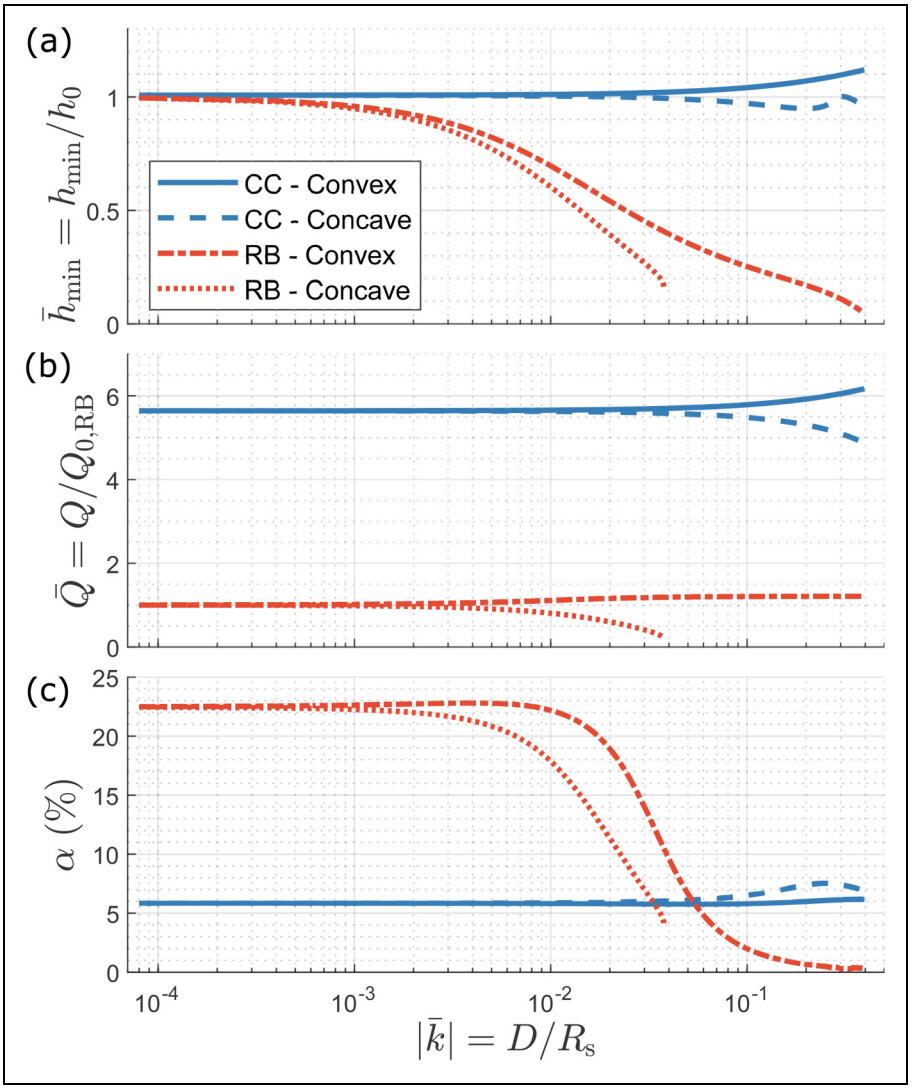

Figure 8. Comparison of the closed cell (CC) and rigid bearing (RB) at the baseline load W_0 on varying curvatures $\bar{k}$ based on (a) minimal film thickness, (b) flow and (c) effective land width α. The flows in (b) are scaled to the flow of RB on a flat surface.

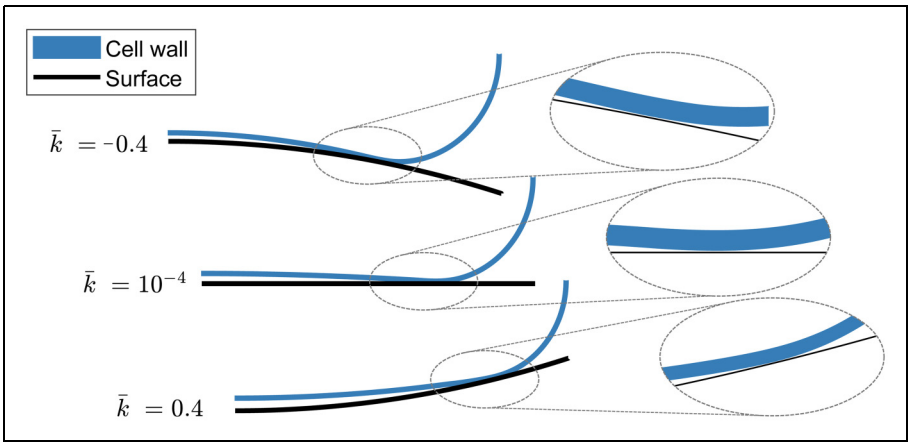

Figure 9. Deformations of the closed cell bearing from the numerical comparison in Figure 8 at the baseline load W_0.

effective land width of both bearings develop for increasing surface curvatures when loaded with the baseline load W_0, which is used to explain the differences in Figure 7. It must be noted that both bearings are initially flat, meaning that their neutral radius of curvature $R_n = \infty$ and the dimensionless surface curvature $\bar{k}$ only depends on R_s.

Examples of the cell deformation at different curvatures from the curvature sweep in Figure 8 are further provided on scale in Figure 9.

At the lower curvatures in Figure 7, similar load capacities are achieved at an equal minimal film height in both bearings, which is to be expected as the restrictor and supply pressure are tuned for an equal fly height at the baseline load. For larger concave curvatures however, the load capacity of the rigid bearing steadily decreases as the surface moves away from the bearing as exemplified in Figure 7(c). As a result, the bearing decreases its film thickness to maintain sufficient film resistance and pressure, which is also seen in Figures 8(a) and (c). Eventually, it only depends on a narrow gap between the surface and the corner between the recess and the land area, which is not sufficient to generate a useful load capacity. A similar effect occurs for increasing curvatures on a convex surface, with the difference that the counter surface moves away from the centre of the bearing and that the narrow gap becomes more concentrated at the outer edges of the bearing. For small curvatures around $\overline{k} = 10^{-2}$ this actually enlarges the recess a bit, which explains the slightly increased load capacity at low film heights in Figure 7(b). For higher curvatures however, the effective land width rapidly decreases again as seen in Figure 8(c).

The blue surfaces in Figure 7 show that the closed cell bearing obtains a more constant load capacity over the range of curvatures, even up to $|\overline{k}| = 0.8$. This constant behaviour is also seen for the different metrics in Figure 8 and is a result of its deformation pattern. On a flat surface, the closed cell already forms a recess as shown in the middle of Figure 9. As a result, its effective land width consists of the relative short narrow gap beneath a segment of the circular part of the cell wall, which results in roughly $\alpha = 0.05$. On the convex and concave surfaces, it is seen in Figure 9 that the cell is able to adapt its bottom wall as described in the expected working principle before, keeping this effective land width and thereby the load capacity constant. A consequence of the small land width though, is a flow rate that is $6\times$ higher than the flow of the rigid bearing. Combined with the supply pressures for this example from Table 1, the required power to operate the closed cell bearing is more then $2.6\times$ higher.

Measurements

Pictures of the prototype in operation and the results of the experimental validation are respectively shown in Figures 10 and 11. During the bearing startup, the fluid first accumulates in the centre, which creates a recess before lifting the entire bearing. On the glass plate in Figure 11(a) however, it is seen that the closed cell eventually forms a complete film beneath its entire surface. On the convex and concave surfaces this is more difficult to verify as the surfaces are not transparent. By visual inspection of the outflow all around the bearing and by manually perturbing the cell wall though, it was

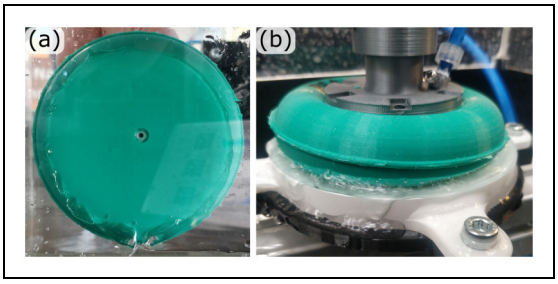

Figure 10. Pictures of (a) the formation of full film beneath the closed cell prototype bearing on a flat glass plate and (b) the prototype on operation on a convex surface.

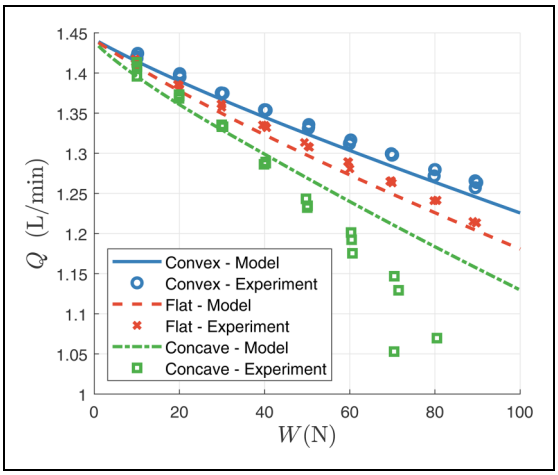

Figure 11. Numerical and experimental flow of the prototype for different load capacities on a flat glass plate and on convex and concave surfaces with $|\overline{k}| = 0.4$.

confirmed that the prototype also formed a full film on the convex and concave test surfaces for the loads that were tested.

The measurements in Figure 11 are in good agreement with the decreasing flow that was predicted by the numerical model for increasing loads. Especially on the flat and convex surfaces the data and model do agree well. The data from the concave surface however shows a diverging trend for loads above 40 N. During the experiment, it was also noted that the cell slowly started to increase in volume when pressed against the concave surface at loads above 50 N. The additional fluid is assumed to have entered the cell from the recess in between the cell wall and the little adapter, that was moulded into it as shown in Figure 6(a), and was removed between measurements. Additionally, it was noted that the cell tends to start shearing out of the centre on convex perturbations at higher loads as seen in Figure 10(b). For these two reasons, the prototype was not tested up to the baseline load W_0 from Table 2 to avoid any more damage.

Discussion

This work aimed to make a first step towards the design of highly deformable fluid film bearings that consist of a

single pad. The study therefore focused, together with the general design requirements and metrics, on introducing the concept of a closed cell bearing support and on analysing its general behaviour to discuss its potential for highly deformable bearings. Hence, optimizations of any design parameters or analyses of other metrics like the bearing stiffness, stability or material stresses have not been presented. The research method used and the potential of the closed cell are further discussed below.

Numerical model and analyses

The work in this study is based on a 2D axi-symmetric design case that is used in the numerical analysis and experimental setup. Cam follower systems however, which form the main example application for highly deformable bearings, only contain a waviness in one direction of the surface. The axi-symmetric design case has nevertheless been used for two reasons. A 2D representation is not physically realizable as the internal fluid is not contained in the out of plane directions and therefore less relevant. A 3D representation though would significantly increase the computational cost, unnecessary for introducing the conceptual idea. Additionally, it is assumed to be easier to make a bearing adapt to a waviness in one direction (i.e. a single curvature) than a double curved surface as presented in this study. The effect of the thin film flow perpendicular to the waviness direction on a single curvature though, should specifically be analysed to prevent a loss of pressure from any undesired high flows in this direction.

With respect to the numerical model, two assumptions are discussed. First of all, it is noted that the Reynolds equation used requires a fully developed laminar flow. The cell wall smoothly bends along with the surface as seen in Figure 9, resulting in a continuous film thickness profile without sharp transitions. The film can therefore be considered as fully developed along the entire domain, which justifies the use of the Reynolds equation. Secondly, the film height has been simplified to the vertical distance between the cell wall and the surface in equation (7). This introduces an error on the curved surfaces as the flow direction is no longer horizontal but becomes more tilted further away from the centre. On a surface with a dimensionless curvature $\overline{k} = 0.8$ for example, the slope becomes 23.6° at the bearing edges, translating to an overestimation of the true, perpendicular film thickness of 9.1%. Due to the relative large difference in film thickness however between the short land width at the edges of the cell and its recess as seen in Figure 9, the influence of this error is rather limited. It should be taken into account though if future designs become able to adapt to longer effective film sizes with more subtle differences in film thicknesses.

With the numerical model, the closed cell was compared to a rigid, recessed thrust bearing. Naturally, this comparison is not entirely realistic as rigid bearings are not designed to operate on varying surface curvatures. It is stressed however that it was only used to show how the closed cell behaves different from the existing, more traditional rigid bearings. A comparison to other single pad deformable bearings from literature was also deliberately not performed. These studies focused on much smaller curvatures for which the overall (external) stiffness of the support was reduced by means of a rubber support.[7–9] To follow larger curvatures however, this approach requires a further reduction of their stiffness which contradicts the design requirement of a high bearing stiffness. These designs have therefore not been simulated on higher curvatures for a comparison to the closed cell.

Experimental

A prototype was built and tested to validate the numerical model, of which the results are shown in Figure 11. Despite the numerous assumptions in the model, the manufacturing of the bearing surfaces with 3D printing techniques and a linear elastic approximation of the material model, the results agree remarkably well with the model. The diverging results on the concave surface are attributed to the leakage into the cell that changed its geometry and therefore its overall behaviour. For future research it is recommended to alter the manufacturing of the recess adapter in the bottom wall to ensure a better sealing between the internal fluid and the film.

Additionally, a modified relation for the orifice restrictor was introduced in equation (8) with an adaptable power f that was fitted for the prototype. The fitted value of $f = 0.58$ confirmed the increased linear behaviour. The low C_d-value of 0.34 further confirmed the decrease in flow resistance due to the rounded edges of the needle entrance, from which it is known in literature that it can half the flow resistance.[18] It must be noted though that the fitted power factor leads to an inconsistency in the units of equation (8), which can be accounted for by adapting the unit of C_d as seen in Table 2.

A final important observation from the experiments is the unintended shearing motion as seen in Figure 10(b). Due to the asymmetry of this deformation, this effect has not been analysed or observed in the axi-symmetric simulations. It is caused by the relative low shear stiffness of the closed cell structure as mentioned in previous research, which allows a rolling motion of the cell that looks like the motion seen in tape loops.[11] Once the formation of a full film beneath the bearing drastically reduces the friction, any perturbation like an eccentricity of the load can easily perturb the cell in its shearing direction. The shearing deformation in Figure 10(b) thus confirms the formation of a full film. However, it also highlights a shortcoming in the current design as (larger) shearing motions affect the bearing performance, could lead to bearing failure and thus limit the load capacity.

Closed cell bearing concept

The results in Figures 7 to 9 show that a closed cell hydrostatic bearing is able to adapt its geometry to different

curvatures and maintain a relative constant effective land width and fly height up to curvatures of at least $|\bar{k}| = 0.8$. The largest surface wavinesses that was previously analysed consisted of a sinusoidal surface with an amplitude of 0.01m and a wavelength of 5πm for a 2m long bearing.[9] This translates to a maximum curvature of $|\bar{k}| = 0.0032$, meaning that the prototype in this study has been shown to work on a surface with a $100\times$ higher dimensionless curvature. The design with a single fluid cell however also shows three limitations.

The first limitation is the pressure difference that arises at the edges of the bearing between the internal fluid and fluid film, as the latter decreases to the ambient pressure. The tension in the cell wall prevents the internal pressure here from squeezing the film entirely. Nevertheless, it still causes the cell to locally form a stronger outwards curvature which results in the relative small effective land width as highlighted in Figure 9. This small effective land width also contributes to the working principle of forming a recess with a different pressure than the internal fluid to curve the pad, but comes with two disadvantages. The first is a lower film stiffness which enlarges the risk of contact with the surface when the load increases. It is questionable though if contact with deformable bearings of more rubbery materials still poses a risk for surface damage and therefore could be more acceptable. The second disadvantage is a higher flow, which already resulted in a $2.6\times$ higher power consumption in the comparison of this study. A better adaptability to increase the effective land width would therefore be desired.

The second limitation is the influence of the material choice and tension in the cell wall on the deformability of the bearing. The cell wall's bending stiffness, related to the bearing's adaptability, scales with $\sim ET^3$ as seen in equation (9), with the Young's Modulus E and wall thickness T. The cell wall's tensile stiffness however, related to the bearing's axial stiffness, scales with $\sim ET$. For an adaptable (i.e. compliant in bending) and axial stiff bearing, it is thus most efficient to reduce the thickness T and to use a material with a high Young's Modulus. A thinner cell wall though, also results in higher tensile stresses in the cell wall that limit the load capacity once the yield stress of the material is reached. A trade-off between the deformability and load capacity of the bearing therefore remains present and for choosing a cell material, one should consider both a high Young's Modulus, high yield stress and the manufacturability into a thin cell wall. For the experimental validation in this study with a relative low load, it therefore sufficed to use a silicone rubber with a thickness of 1.5 mm. Additionally, higher loads on the bearing cause a higher internal pressure and thus a higher tension in the cell wall. This tension also increases the deformation stiffness of the cell that initially only depends on the wall's flexural rigidity.

The third limitation is the relative low shear stiffness of the current design, as mentioned in the experimental discussion. At higher loads this poses a risk of instability as the closed cell support could slip away between the load and surface. Shear stiffness improvements are therefore required to make the concept feasible for high loads.

Conclusions

This work introduced three general requirements and two performance metrics for the development of deformable fluid film bearings that can operate on surfaces with a significant and varying curvature. With minimal literature on this topic, the requirements form a basis to help narrow down and focus the solution space in a viable direction. The metrics hereby assist to assess current and future solutions in a universal manner independent of their scale. Additionally, this work presented a closed fluid cell as a design element for highly deformable fluid film bearings. The combination of a fluid that is enclosed by a thin cell is able to combine a high load capacity and bearing stiffness with the deformability to adapt to varying curvatures. The FEM model that was developed for the implementation of such a cell as a hydrostatic bearing showed a good agreement with validation measurements on a prototype and provides a method to further analyse such bearings. The prototype also confirmed that curvatures of $|\bar{k}| = 0.4$ already can be followed with the proposed design in a 2D axi-symmetric design case. Enclosed fluid cells are therefore promising to further develop deformable fluid film bearings. Primary future objectives are the development of supports that result in smaller effective land widths.

Data availability

The research data related to this publication is available in the 4TU.ResearchData repository, DOI: 10.4121/26a9bd64-fa73-4d24-8bdd-d502ffe1aa49.

Declaration of conflicting interests

The authors declared no potential conflicts of interest with respect to the research, authorship, and/or publication of this article.

Funding

The author(s) disclosed receipt of the following financial support for the research, authorship, and/or publication of this article: The research was funded by the Topsector Energy Subsidy of the Dutch Ministry of Economic Affairs (TEHE119007).

ORCID iDs

Dave D. Sonneveld https://orcid.org/0000-0001-7288-6902
Ron A.J. van Ostayen https://orcid.org/0000-0002-4814-544X

References

1. Diepeveen NFB, Jarquin Laguna A and Kempenaar AS. Water-hydraulic power transmission for offshore wind farms. In: *Proceedings of the dutch fluid power conference 2012*, 2012, Ede, The Netherlands: Vereniging Platform Hydrauliek.
2. Diepeveen NFB. *On the application of fluid power transmission in offshore wind turbines*. PhD Thesis, Delft University of Technology, Delft, 2013.

3. Chen W, Wang X, Zhang F, et al. Review of the application of hydraulic technology in wind turbine. *Wind Energy* 2020; 23: 1495–1522.
4. Nijssen J, Kempenaar A and Diepeveen N. Development of an interface between a plunger and an eccentric running track for a low-speed seawater pump. In: *11th International fluid power conference*, Vol. 1, 2018, pp.370–379. Aachen, Germany: RWTH Aachen University. DOI: 10.18154/RWTH-2018-224521.
5. van Beek A and Segal A. Rubber supported hydrostatic thrust bearings with rigid bearing surfaces. *Tribol Int* 1997; 30: 47–52.
6. Liang X, Yan X, Ouyang W, et al. Thermo-elasto-hydrodynamic analysis and optimization of rubber-supported water-lubricated thrust bearings with polymer coated pads. *Tribol Int* 2019; 138: 365–379.
7. van Beek A and Lepic L. Rubber supported hydrostatic thrust bearings with elastic bearing surfaces of infinite length. *Wear* 1996; 201: 45–50.
8. van Ostayen RAJ, van Beek A and Ros M. A parametric study of the hydro-support. *Tribol Int* 2004; 37: 617–625.
9. Nijssen JPA and van Ostayen RAJ. Compliant hydrostatic bearings utilizing functionally graded materials. *J Tribol* 2020; 142: 111801.
10. van Parijs V, Nijssen J and van Ostayen R. Whiffletree based supports for self-adjustable hydrostatic bearings. *Adv Mech Eng* 2021; 13 DOI: 10.1177/16878140211055573.
11. Sonneveld DD, Nijssen JP and van Ostayen RA. Compliant joints utilizing the principle of closed form pressure balancing. *J Mech Design* 2023; 145: 083601.
12. Lugt PM and Morales-Espejel GE. A review of elasto-hydrodynamic lubrication theory. *Tribol Trans* 2011; 54: 470–496.
13. Howell LL. Compliant mechanisms. In: *21st Century kinematics*, 2013, pp.189–216. London: Springer. DOI: 10.1007/978-1-4471-4510-3_7.
14. Michalec M, Svoboda P, Krupka I, et al. A review of the design and optimization of large-scale hydrostatic bearing systems. *Eng Sci Technol Int J* 2021; 24: 936–958.
15. Rowe WB. *Hydrostatic, aerostatic and hybrid bearing design*. 1st ed. Oxford: Elsevier, 2012.
16. Gomes RFP, Nijssen JPA and van Ostayen RAJ. Design of a compliant hinge based on closed form pressure balancing. In: *Proceedings of the ASME 2020 international design engineering technical conferences and computers and information in engineering conference*, Vol. 10, 2020, p.V010T10A003. 44th Mechanisms and robotics conference (MR). American Society of Mechanical Engineers. DOI: 10.1115/DETC2020-22100.
17. COMSOL Multiphyscis®. V. 6.1. COMSOL AB, Stockholm, Sweden. Available online: www.comsol.com (accessed 7 June 2024).
18. van Beek A. *Advanced engineering design: Lifetime performance and reliability*. 6th ed. Delft: Delft University of Technology, 2015.